Check for updates

Modelling second harmonic generation at mid-infrared frequencies in waveguide integrated Ge/SiGe quantum wells

GIOVANNI CHESI,[1] VIRGINIA FALCONE,[2] STEFANO CALCATERRA,[2] MICHELE VIRGILIO,[3,*] AND JACOPO FRIGERIO[2] (iD)

[1]*INFN, Sezione di Pavia, Via Agostino Bassi 6, I-27100 Pavia, Italy*
[2]*L-NESS, Dipartimento di Fisica, Politecnico di Milano, Polo Territoriale di Como, Via Anzani 42, I-22100, Como, Italy*
[3]*Diprtimento di Fisica"E. Fermi", Università di Pisa, Largo Pontecorvo 3, I-56127 Pisa, Italy*
michele.virgilio@unipi.it

Abstract: A promising alternative to bulk materials for the nonlinear coupling of optical fields is provided by photonic integrated circuits based on heterostructures made of asymmetric-coupled quantum wells. These devices achieve a huge nonlinear susceptivity but are affected by strong absorption. Here, driven by the technological relevance of the SiGe material system, we focus on Second-Harmonic Generation in the mid-infrared spectral region, realized by means of Ge-rich waveguides hosting p-type Ge/SiGe asymmetric coupled quantum wells. We present a theoretical investigation of the generation efficiency in terms of phase mismatch effects and trade-off between nonlinear coupling and absorption. To maximize the SHG efficiency at feasible propagation distances, we also individuate the optimal density of quantum wells. Our results indicate that conversion efficiencies of $\approx 0.6\%/W$ can be achieved in WGs featuring lengths of few hundreds μm only.

1. Introduction

Photonic integrated circuits (PICs) working in the Mid-infrared (MIR) have received in the last years a great attention due to the variety of potential applications in medical diagnostics [1], analytical chemistry [2], environmental monitoring [3], and sensing for safety and security [4]. The interest toward the MIR is motivated by the presence in this spectral region of unique vibrational "fingerprints" of many molecules, that allows their detection in a label-free approach. Quite recently, research efforts in the field of MIR photonics targeting the realization of automated MIR molecular sensors with high molecule specificity [6] have been boosted also by the commercial availability of wavelength-tunable MIR quantum cascade lasers (QCLs) [5]. Key applications include the atmospheric sensing of carbon dioxide and monoxide, the determination of protein conformational states, and the quantification of specific molecules in blood or saliva for rapid health monitoring. From a more general perspective, the development of non-linear optical devices is essential for applications in all-optical signal processing [7], spectroscopy [8] and quantum optics [9,10]. In particular, second-order nonlinear phenomena are key to achieve high-speed optical modulation via the Pockels effect [11], f-2f frequency-comb self-referencing [12], and also direct frequency-comb generation by cascaded second-order effects that mimic third-order nonlinear effects, but with higher efficiency [13].

Many research efforts have been dedicated to achieve second-order nonlinearities in silicon PICs. To this aim, the SiGe material system represents a natural choice, thanks to its prompt integrability with the CMOS standard. Indeed bulk Si and Ge are compatible with PIC foundry processes [14,15], but unfortunately both feature vanishing second-order susceptibility $\chi^{(2)}$ due to their centrosymmetric unit cell. To circumvent this limitation it has been observed that an external

electric field induces nonlinearity in periodically poled silicon-on-insulator (SOI) waveguides, but the reported $\chi^{(2)}$ values were limited to less than 1 pm/V [16]. Slightly larger $\chi^{(2)}$ (2.5 pm/V) has been demonstrated in SHG experiments performed with Si_3N_4 waveguides [17] and micro-resonators [18], both on SiO_x. Also strain-induced second-order nonlinearities have been demonstrated on the SOI platform, reaching a $\chi^{(2)}$ of 40 pm/V [19]. However, the transparency range of SOI and Si_3N_4 waveguides is limited to wavelengths $\lambda < 4\,\mu m$, due to the onset of strong phonon absorption in SiO_x [20,21,22]. Interestingly, also the integration of conventional non-linear crystals on silicon is progressing steadily with several non-linear optical effects recently demonstrated in $LiNbO_3$-on-insulator (LNOI) [23,24] and GaAs-on-insulator [25]. Nevertheless, also in this case the presence of the SiO_2 material make the low-wavelength part of the MIR inaccessible. To overcome this limitation, unconventional strategies leveraging on nanostructures with strain gradients [26] or on non-linear free-electron plasma oscillations in heavily doped Si or Ge [27,28] have been recently reported. However, the proposed nanostructures are difficult to realize in a controlled manner, while the efficiency in heavy doped crystals is severely limited by high ohmic losses. Therefore, the development of Si compatible materials able to provide robust second-order nonlinearities at longer wavelengths is still an open challenge.

As an alternative approach toward this objective, in this paper we theoretically investigate second harmonic generation in SiGe waveguides (WGs) grown on Si and hosting a periodic stack of p-type Ge/SiGe asymmetric-coupled quantum wells (ACQW). In fact, such heterostructures can be specifically tailored to realize double resonant intersubband transitions (ISBTs) which, thanks to their large oscillator strength, guarantee a great enhancement of the second harmonic generation effect. As a matter of fact, for this kind of system, giant $\chi^{(2)}$ coefficients are expected, with values typically in the 10^4-10^5 pm/V range [29]. This approach has been widely investigated more than two decades ago in III-V quantum wells [30,31,32] and it has been recently revisited using metasurfaces [33–36] providing strong field enhancement. Our choice of a hole-based device is related to the fact that the Ge/SiGe interface features a larger valence band off-set with respect to the conduction one [37], making p-type ACQW suited to work in the long-wave infrared (LWIR) spectral region ($\lambda = 8$-$12\,\mu m$). Having in mind the design degrees of freedom, to maximize the SHG efficiency in our modelling we have accurately taken into account the optical attenuation related to the linear absorption of pump and 2ω photons, caused by ISBTs. Indeed, this physical effect represents the main drawback of non-linear optical amplification when leveraging on QW nanostructures and must be properly considered to identify the optimal waveguide length. To this aim, after calculating the optical properties of the heterostructure in terms of second-order non-linear susceptibility $\chi^{(2)}$, optical absorption and refractive index, we have investigated the maximum conversion efficiency as a function of the pump wavelength, the number of ACQW and the WG length. Our results show that the proposed WGs can provide conversion efficiencies around 0.6%/W for propagation lengths of few hundreds of μm.

The paper is organized as follows: in the Section 2 we present the heterostructure together with its electronic and optical properties. The Section 3 is dedicated to the WG design and modelling. The model used to calculate the SHG efficiency as a function of the propagation length is discussed in the fourth Section; Then, in section 5, our model is used to predict SHG in different rib WGs, which share the same geometry but differ by the number of embedded ACQW, considering both phase-matching (PM) and phase-mismatched (non-PM) conditions. In the sixth section we discuss the results. Finally, in the last Section, we compare our material system with other platforms.

2. Electronic and optical properties of the ACQWs

The chemical profile of the ACQWs embedded in the WG here investigated is equal to the one discussed in Ref. [29]. The periodically repeated ACQWs layers consists of a 2.4 nm $Si_{0.07}Ge_{0.93}$ p-doped main well, with acceptor density of $1 \times 10^{18}\,cm^{-3}$, followed by a 1 nm

Si$_{0.33}$Ge$_{0.67}$ tunnelling barrier coupling a 2.7 nm thick Si$_{0.24}$Ge$_{0.76}$ secondary well, and finally by a 3.9 nm Si$_{0.48}$Ge$_{0.52}$ main barrier which separate each module of this periodic quantum region (see Fig. 1(a)). Since Si and Ge are completely miscible over the full compositional range, unavoidable interdiffusion effects tend to smooth the compositional (and consequently also the potential) profile of the heterostructure. As it is apparent from Fig. 1(b), to improve the accuracy of the model, we have taken into account this effect, by using a chemical profile experimentally measured by high-resolution X-ray diffraction and transmission electron microscopy [29]. Notice that to achieve compensation between the compressive and tensile strain field present in the well and barrier material, respectively, the ACQW stack is designed to be lattice matched with a Si$_{0.3}$Ge$_{0.7}$ relaxed virtual substrate, which we introduce to minimize the elastic energy stored in the epilayers.
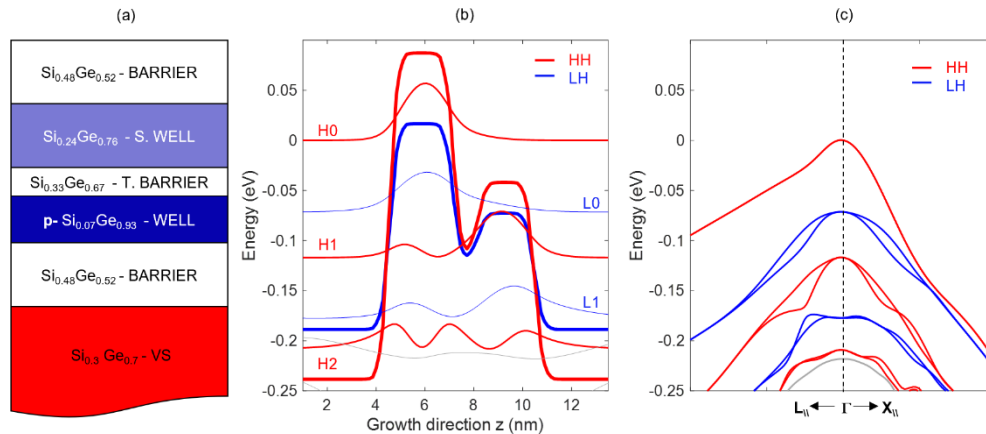

Fig. 1. Epitaxial scheme of the sample (a). Heavy (red) and light (blue) band edges profiles of the ACQW together with the squared wavefunctions associated to the HH and LH bands (b). ACQW band-structure in a neighbor of the Γ point (c).

As a first step, we calculated the electronic band structure using a well established semi-empirical first-neighbor $sp^3d^5s^*$ tight-binding Hamiltonian model which includes also the spin-orbit interaction (see Ref. [38,39]). This multi-orbital description ensures that all the relevant effects related to the subband non-parabolicity and to the momentum-dependence of the dipole matrix elements, which for p-type structures operating at room temperature (RT) are expected to play a relevant role, are properly considered. The valence band edge potential profile for the heavy-hole (HH) and the light-hole (LH) bands, together with the respective wavefunctions H$_i$ and L$_i$ is reported in Fig. 1(b). The fundamental state H$_0$ originate from the HH band and for reference its energy has been set at 0 eV. The electronic spectrum in a neighbor of the Γ point is shown in Fig. 1(c) and as expected, due to their interaction, the HH and LH subbands are not parallel. The heterostructure features three confined HH subbands: the ground state H$_0$, tightly confined in the deeper well and the excited H$_1$ (-0.115 eV) and H$_2$ (-0.207 eV) levels, which extend also in the secondary well. Consequently, the symmetry selection rule which for square QW systems suppresses the H$_0$ →H$_2$ transition for TM light due to parity violation, does not apply in our case. In other words, thanks to the asymmetry artificially produced by the chemical profile which defines our ACQWs, H$_0$ →H$_1$ and the H$_0$ →H$_2$ ISBs are both active. Indeed, the resonant SHG process in our system leverages just on these transitions and, in order to maximize its effectiveness, we have engineered the involved states so to achieve robust dipole matrix elements and very similar values for the E$_{10}$ and E$_{21}$ energies. Regarding the LH band, the L$_0$ level, which is confined in the main well, lies at -0.071 eV, while the excited L$_1$ level is found at -0.177 eV. It follows that at RT the great majority of hole carriers populate only the

H_0 subband, the other subbands being quite far in energy with respect to kT. The spectrally resolved $\chi^{(2)}_{(ikj)}$ tensor has been calculated sampling in a neighbor of the Γ point the Brillouin zone of the ACQW, so to properly account for both the non-parallel subband dispersion and the k-dependence of the dipole matrix elements. Moreover, in the evaluation of $\chi^{(2)}_{(ikj)}$, beside the resonant term associated to the degeneracy of E_{10} and E_{21}, we have considered also all the anti-resonant contributions (see Ref. [38] for more details).

Notice that dipole matrix elements for ISBT in hole doped QWs are not aligned along the growth direction z, as instead happens for n-type systems with a diagonal effective mass tensor. In this latter case the only non-vanishing component of the second order susceptivity tensor is $\chi^{(2)}_{(zzz)}$. Our system instead exhibits non negligible values also for the off-diagonal terms of $\chi^{(2)}_{(ikj)}$. This fact can be exploited to design vertical illuminated devices where the photon beams are polarized in the growth plane *xy* as discussed for instance in Ref. [26]. In the present work however we target integrated devices and thus, since the largest susceptivity is related to the $\chi^{(2)}_{(zzz)}$ component, we have designed our WG to support a TM polarized mode i.e. a radiative electric field which oscillates along the z direction both for the pump and SH fields. Here we should point out that the $\chi^{(2)}_{(xzz)}$ and $\chi^{(2)}_{(yzz)}$ components of the tensor are vanishingly small, so we don't expect any pump depletion from SHG generation toward TE modes. Therefore in the following we limit our discussion to $\chi^{(2)}_{(zzz)}$ (just $\chi^{(2)}$ from now). Its spectral shape, shown has a function of the wavelength associated to input photons of angular frequency ω is shown in Fig. 2(a). As expected, we find a well-defined resonance, at 12 µm, corresponding to 103 meV, a value at the center of the energy interval defined by the E_{10} (115 meV) and E_{21} (92 meV) transition energies. We also notice that it is present also a small secondary peak, centered at 7.5 µm, which we associate to the presence of the $H_0 \rightarrow L_1$ ISBT. As mentioned in the introduction, to improve the accuracy of the predicted SHG efficiency for the proposed WGs, we have included in our model also depletion effects due to the absorption of ω and 2ω photons. To this aim we have calculated for TM polarization the spectral shape at RT of α_{QW} which represents the contribution to the total linear absorption α brought about by the ISBTs occurring in the ACQWs. For this purpose, we follow the approach described in [38]. Our results are reported in Fig. 2(b) (dotted line). In the same plot we also show the contribution to the linear absorption due to the presence of free carrier α_{FCA}, (dashed line in Fig. 2(b)), caused by the p-doping in the main well. The spectral shape of α_{FCA} has been calculated using the relation [40]:

$$\alpha_{FCA}(\lambda) = c(\lambda) \cdot N_a^{d(\lambda)}, \tag{1}$$

where the wavelength-dependent coefficients c(λ) and d(λ) have been taken from the experimental data available for Ge [41] and Si [42] and have been linearly interpolated with the Ge concentration to estimate the appropriate values for the SiGe alloy material. We notice that the above Equation refers to FCA in bulk crystals and has been adopted here due to the lack of experimental data about 2D FCA in Ge/SiGe QWs. The total absorption coefficient $\alpha = \alpha_{QW} + \alpha_{FCA}$ of the ACQW as a function of the wavelength is reported in Fig. 2(b) (solid line). The absorption spectrum is dominated by a broad peak located at $\lambda = 10.7$ µm (hν = 116 meV) which is to be attributed to the $H_0 \rightarrow H_1$ ISBT while at lower wavelengths we distinguish also spectral features due to the $H_0 \rightarrow L_1$ ($\lambda = 7.7$ µm, hν = 161 meV) and to the $H_0 \rightarrow H_2$ ($\lambda = 6$ µm, hν = 207 meV) ISBTs. Finally, the high energy shoulder present at lower wavelength has been attributed to ISBTs from H_0 to the HH continuum.

To describe the interaction of the pump and second harmonic radiative fields propagating in the WG, we also preliminary need to estimate the refractive index *n* of the *p*-type ACQW material which, due to the presence of the ISBTs features a nontrivial wavelength dependence in this spectral region. Its value has been calculated adding to the value n_{bulk} of a $Si_{0.3}Ge_{0.7}$ bulk material the contribution Δn_{QW} brought about by the ISBTs ($n = n_{bulk} + \Delta n_{QW}$). This latter quantity has been obtained from the absorption spectrum by applying Kramers-Kronig
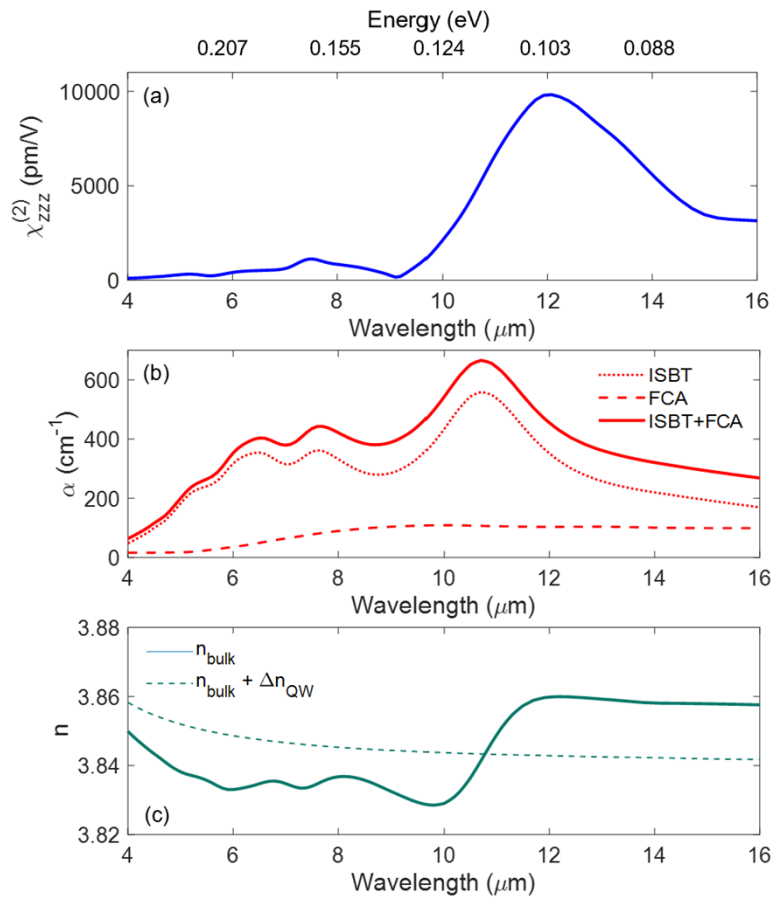
Fig. 2. $\chi^{(2)}{}_{(zzz)}$ (a), absorption coefficient (solid) resulting from the contribution of FCA (dashed) and ISBT (dotted) (b) and refractive index (c) of the ACQW, as a function of the wavelength (bottom axis) and of the photon energy (top axis).

transformations. As apparent from Fig. 2(c), in the spectral region of interest we obtain deviation from n_{bulk} of the order of 0.5%, which can be interpreted as due to the anomalous dispersion associated to the $H_0 \to H_1$ absorption resonance centered at $\lambda = 10.7$ μm. The perturbation induced by the ACQWs on the refractive index (and consequently on the phase mismatch between the pump and SH fields) is rather weak, nevertheless we will include it in the model (as explained below) to strengthen its reliability.

3. Modelling of the optical modes in the waveguide

Having addressed the optical properties of the active part of the envisioned non-linear WGs, we now discuss in more detail their geometrical shape and compositional profile. As a matter of fact, the proposed WG integration of Ge/SiGe ACQWs requires a Ge-rich SiGe buffer that acts as a fully relaxed VS. This layer allows the growth of high quality ACQWs and, at the same time, serve as low loss guiding material. Due to the large lattice mismatch with the Si substrate, the growth of the VS layer is not trivial. Indeed, this challenge has been tackled only recently to demonstrate WG integrated intensity modulators working at near-infrared wavelengths [43]. The strategy adopted by the Authors of Ref. [43] leveraged on the introduction of few μm thick SiGe linear graded buffers layers (GB) deposited on Si, resulting in a suppression of the crystal

defect density caused by the accumulation of the elastic energy. This approach has a positive side effect for MIR applications since the increasing of the refractive index along the growth direction associated to the graded Ge concentration push upward the confined optical mode. In this way its overlap with the lossy Si substrate, whose transparency is limited to $\lambda < 8$ μm, is greatly suppressed [44]. In light of the above considerations, we propose the rib WG geometry reported in Fig. 3(a), which has been optimized to support single mode operation in TM polarization between $\lambda = 5$ μm and $\lambda = 12$ μm, so to enhance the oscillator strength of ISBTs involving HH subbands. The WG has been designed by using the finite difference method, as implemented in the package MODE of the Lumerical software. The buffer layer consists in a linearly graded $Si_{1-y}Ge_y$ region where the Ge concentration y is raised from 0 to 69% with a grading rate of 7%/μm. The GB is followed by a 2 μm thick $Si_{0.3}Ge_{0.7}$ constant composition layer, which serves as VS for the ACQWs.
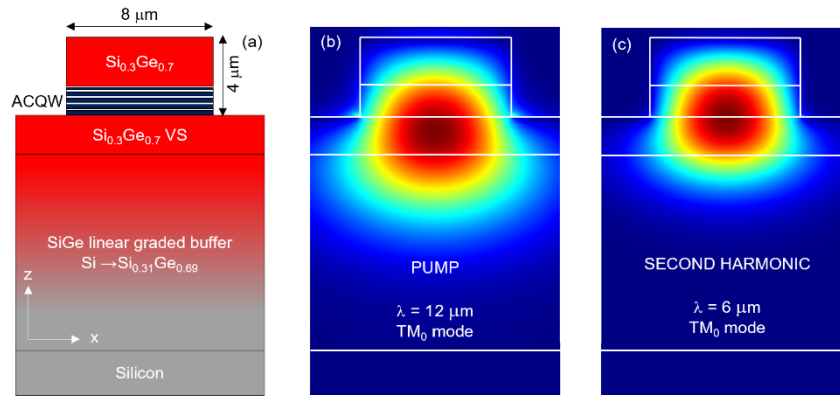

Fig. 3. Rib waveguide geometry with N = 100 repetitions of the ACQW module (a). Spatial distribution of the TM_0 optical mode in the WG at $\lambda = 12$ μm (pump wavelength) (b) and at $\lambda = 6$ μm (second harmonic wavelength) (c).

The WG core stack consists of *N* repetitions of the ACQW module, with *N* chosen in the 1-200 range. The ACQW have been modelled in MODE as a custom material using the refractive index reported in Fig. 2(c). The final part of the structure consists in a constant composition $Si_{0.3}Ge_{0.7}$ layer whose thickness is adjusted to achieve a constant WG height of 4 μm. The calculated optical mode distributions, effective indices, and overlap factors have been used as input parameters to model the SHG efficiency, as detailed in the next Sections. As an exemplary case, we report in panel (b) and (c) of Fig. 3 the TM mode calculated at λ=12 μm and λ=6 μm, respectively for $N = 100$, a value corresponding to a total ACQWs thickness of 1.5 μm. As apparent from the plots, we point out that, thanks to the presence of the graded VS, the interaction of the radiative field with the Si substrate is practically negligible.

4. Modelling of second harmonic generation

Our model for SH propagation exploits a perturbative approach to the wave equation for the electric field. In particular, we follow De Leonardis and Soref [45] which, similarly to our case, have described SHG in WGs embedding Si-GaP ACQWs. The equations for the evolution of the electric field amplitudes along the propagation direction *y* in the presence of absorption and mismatch can be retrieved from the nonlinear coupled mode theory [46] and yield:

$$\frac{dE_\omega}{dy} = -\Gamma_\omega \alpha_\omega E_\omega + i\sqrt{2}\Gamma_{112} \sqrt[4]{\frac{\mu_0}{\varepsilon_0}} \frac{\omega}{cn_{eff,\omega}\sqrt{n_{eff,2\omega}}} \chi_{zzz}^{(2)} E_{2\omega}E_\omega^* e^{i\Delta k \cdot y}, \qquad (2)$$

$$\frac{dE_{2\omega}}{dy} = -\Gamma_{2\omega}\alpha_{2\omega}E_{2\omega} + i\sqrt{2}\Gamma_{112} \sqrt[4]{\frac{\mu_0}{\varepsilon_0}} \frac{\omega}{cn_{eff,\omega}\sqrt{n_{eff,2\omega}}} \chi_{zzz}^{(2)} E_\omega^2 e^{-i\Delta k \cdot y}, \tag{3}$$

where E is the electric field, $n_{eff,\omega}$ is the effective index at angular frequency ω, α is the absorption coefficient and Γ is the overlap factor between the electric field and the ACQW region (the subscripts ω and 2ω indicate the pump and the second harmonic wavelength, respectively). WG propagation losses are not taken into account here, since in SiGe WGs they are three orders of magnitude lower than those due to the combined FCA and ISBT contributions (typically $\alpha_{prop} \approx 0.5\,cm^{-1}$ [47]). In the above equations $\Delta k = 2\omega(n_\omega - n_{2\omega})/c$ represents the phase mismatch. Γ_{112} is the overlap factor between E_ω^2 and $E_{2\omega}$, and it is expressed as:

$$\Gamma_{112} = \int\!\!\!\int\limits_{-\infty}^{+\infty} \tilde{E}_\omega^2(x,z)\tilde{E}_{2\omega}(x,z)\, A(x,z)dxdz, \tag{4}$$

where $\tilde{E}_\omega^2(x,z)$ and $\tilde{E}_{2\omega}(x,z)$ are the normalized spatial distributions of the square of the pump electric field E_ω^2 (x,z) and of the second harmonic electric field $E_{2\omega}(x,z)$, respectively, which have been derived from the output of MODE. $A(x,z)$ is a function equal to 1 in the region where the ACQWs are present, and equal to 0 elsewhere. The figure of merit we use here is the SHG conversion efficiency normalized over the input power $P_\omega(y=0)$, expressed in %/W:

$$\eta(y) \sim = \frac{100 * P_{2\omega}(y)}{P_\omega^2(0)}, \tag{5}$$

where $P_{2\omega}$ is the power associated to the SH radiative field. As a first step, we investigate the optimal pump wavelength λ_{opt} that maximizes the SHG efficiency, resulting from the competing contributions of the resonant second-order nonlinear susceptibility and of the optical absorption.
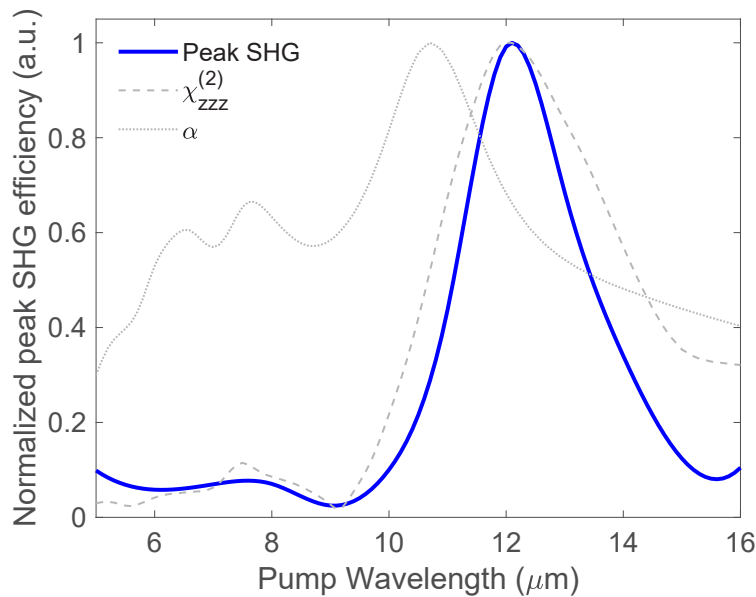

Fig. 4. Plot of the normalized SHG efficiency as a function of the pump wavelength (solid line). The dependence of the efficiency on the wavelength is compared with the ones of the normalized susceptivity (dashed line, arb. units) and of the absorption (dotted line, arb. units).

Table 1. Main WG parameters, as calculated by MODE.

N ACQW	Γ_ω	$\Gamma_{2\omega}$	Γ_{112}	$n_{\mathrm{eff},\omega}$	$n_{\mathrm{eff},2\omega}$
1	0.0019	0.0029	0.0027	3.7463	3.8151
5	0.0116	0.0182	0.0169	3.7463	3.8149
10	0.0231	0.0363	0.0335	3.7463	3.8146
25	0.0556	0.0877	0.0798	3.7463	3.8139
50	0.1048	0.1658	0.1469	3.7464	3.8127
100	0.1813	0.2837	0.2385	3.7464	3.8107
200	0.2504	0.3681	0.2902	3.7464	3.8089

By numeric integration of Eqs. (2) and (3), the optimal wavelength, which does not depend on the number N of ACQW, is found to be $\lambda_{\mathrm{opt}} = 12.1\ \mu$m, (see Fig. 4), practically coincident with the $\chi^{(2)}$ peak. Here it should be made clear that this result is peculiar of the sample investigated in this work. Indeed, the slight detuning of the $H_0 \rightarrow H_1$ and the $H_1 \rightarrow H_2$ ISBTs causes a shift between the $\chi^{(2)}$ peak, whose spectral shape depends on both transitions, and the main peak of the optical absorption α, which depends only on the $H_0 \rightarrow H_1$ ISBT. In the ideal case of perfectly resonant ISBTs, the $\chi^{(2)}$ and α peaks would be at the same wavelength, and we would have found λ_{opt} significantly detuned from it. Having set the pump wavelength, we can now calculate by MODE the main parameters of the model for different repetition N of the ACQW period, as reported in Tab. 1. The overlap factor between the pump electric field and the ACQW region Γ_ω goes from 0.19% for N = 1 to 25.04% for N = 200. Also $\Gamma_{2\omega}$ (Γ_{112}) shows a monotonous trend, going from 0.29% (0.27%) for N = 1 up to 36.81% (29.02%) for 200 ACQW repetitions. The effective index $n_{\mathrm{eff},\omega}$ at the pump wavelength remains substantially unchanged as N increases. This is due to the considerable dimension of the optical mode at $\lambda \approx 12\ \mu$m, which extends significantly into the graded buffer region (see Fig. 3(b)), and to the fact that the variation of the material refractive index caused by the ACQWs contribution is almost zero at the pump wavelength (see Fig.2c). This is not true at the SH frequency 2ω for which the effective index $n_{\mathrm{eff},2\omega}$ shows a (weak) dependence on N, slightly decreasing as N increases. In line with the above considerations, we attribute this trend to a smaller extension of 2ω optical mode, resulting in a larger overlap with the N-dependent ACQW region and to the greater impact of the ACQW on the material refractive index (at the SH wavelength $\Delta n_{QW} < 0$). This small variation of the effective refractive indexes, together with the enhancement of the overlap factors for increasing N determines a change in the optimal propagation distance y_{opt}, i.e. the position of the efficiency peak, as we will show in the next Section.

5. SHG efficiency

In this Section we evaluate the SHG efficiency by numeric integration of Eqs. (2) and (3) in perfect PM conditions (i.e. artificially setting $\Delta k = 0$) and in presence of phase mismatch. Here it has to be mentioned that the PM condition in WG integrated ACQWs could be achieved by different methods, including refractive index engineering [48] and WG shape modulation [49]. An in-depth analysis of these methods would require a full three-dimensional modelling of the WG using the finite difference time domain method.

Such analysis is beyond the scope of this paper, and it will be addressed in a future dedicated work. In Fig. 5, to better highlight the role played by optical absorption in this material, we also show the optical power in the case of a lossless material. In presence of absorption, the SH power increases with the WG length *y* until it reaches a maximum, which occurs when the pump is almost fully depleted, then it decays abruptly, due to the strong SH absorption. In the case of a lossless material, on the contrary, the SH fully depletes the pump until it reaches a maximum
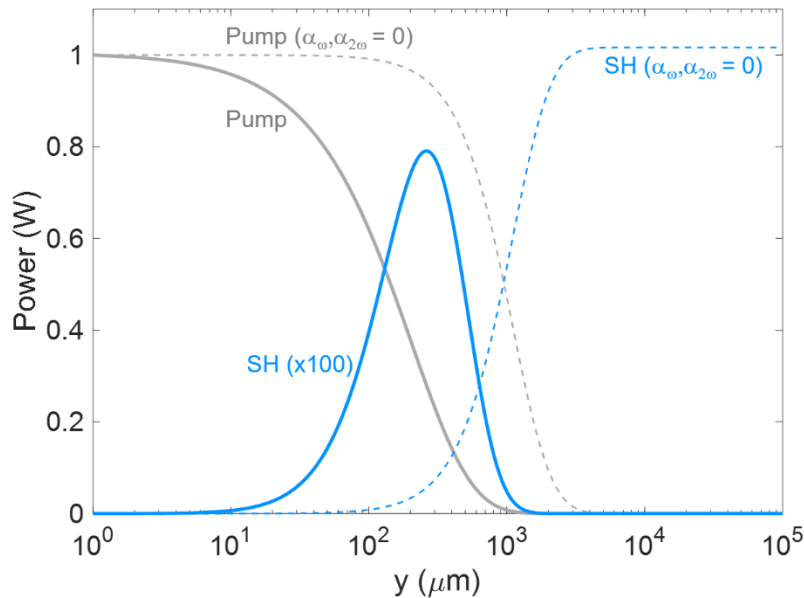
Fig. 5. Pump (grey) and 100x SH (light blue) power as a function of the propagation length with (solid lines) and without (dashed lines) optical absorption. The calculations have been performed considering N = 50 ACQWs.

power (which is slightly higher than the pump because of the smaller modal area of the SH field), which is then manteined thanks to the absence of optical absorption. In Fig. 6 we show the SH efficiency η as a function of the propagation length y for different number N of ACQWs embedded in the WG in PM conditions. Interestingly we notice that the peak efficiency increases for decreasing N, with a maximum efficiency of $\eta = 0.63\%/W$ with N = 1 ACQW. There is a trade-off between the maximum efficiency η and the optimal propagation length y_{opt}, but we see a clear advantage in exploiting a large number of ACQWs. Indeed, even if choosing N < 25 allows to achieve a larger maximum of the SHG efficiencies, we find that it requires propagation distances of few mm, thus losing one of the main advantages of the ACQW technology. On the other hand, at the price of losing the 30% of the peak efficiency at most, increasing the number of ACQWs allows to achieve propagation distances of few hundreds of μm, two orders of magnitude smaller than in the previous case.

When non-PM condition is considered, the SHG efficiency as a function of propagation length shows a periodic trend, with multiple peaks, whose amplitude is damped by the optical absorption, as it can be seen in Fig. 7. In this case the SH conversion efficiency clearly increases by increasing the number of ACQW, reaching a maximum η of $0.41\%/W$ for N = 100, with a propagation length of only 130 μm. Interestingly, we also notice that the difference between the maximum efficiency reachable in PM and not-PM conditions reduces as N increases, because for large N the peak efficiency is reached at propagation lengths significantly shorter than the coherence length y_{CO}, which is of ≈ 600 μm for N = 200.
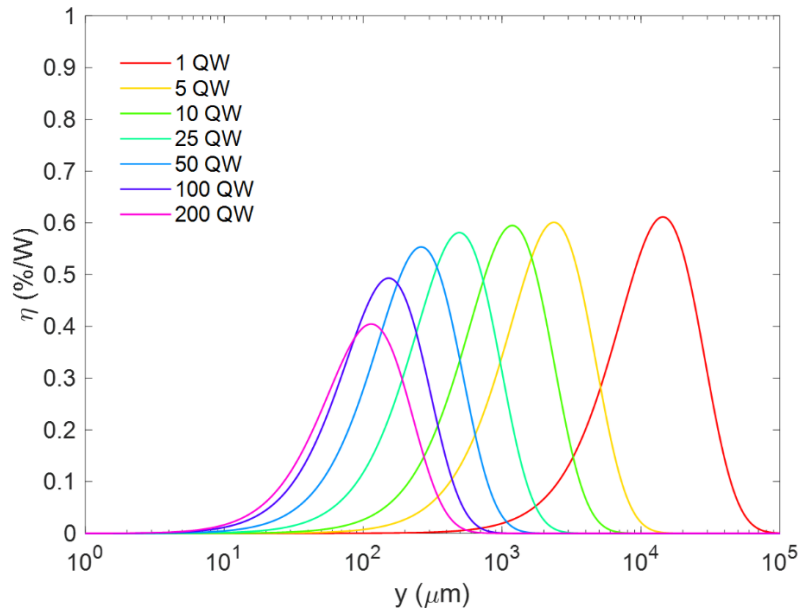
Fig. 6. SHG efficiency in phase-matching condition, as a function of the propagation length for different repetitions N of the ACQW period.
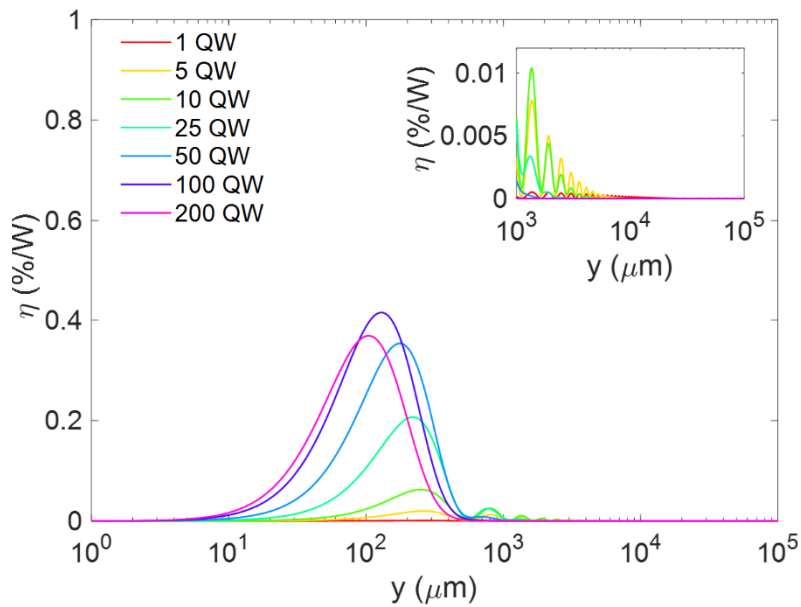

Fig. 7. SHG efficiency with phase mismatch, as a function of the WG length for different repetitions N of the ACQW period. The oscillation of η as a function of the propagation length can be observed in the inset.

6. Discussion

Finally, we provide a qualitative physical interpretation of the results obtained by numerical integration of the equations governing the coupling of the two optical modes. In particular, we are interested in understanding the peculiar dependence of the SH efficiency as a function of the number of ACQWs. To this aim we notice that the differential Eqs. (2) and (3) can be analytically solved by neglecting the back-conversion term in Eq. (2), which is a common approximation in this context. The SHG efficiency in this case reads:

$$\eta(y) = \frac{2\Gamma_{112}{}^2 \sqrt{\frac{\mu_0}{\varepsilon_0}} \frac{\omega^2}{c^2 n_\omega^4} (\chi_{zzz}^{(2)})^2}{(2\Gamma_\omega \alpha_\omega - \Gamma_{2\omega} \alpha_{2\omega})^2 + (\Delta k)^2}$$

$$*[e^{-4\Gamma_\omega \alpha_\omega y} + e^{-2\Gamma_{2\omega} \alpha_{2\omega} y} - 2e^{-(2\Gamma_\omega \alpha_\omega + \Gamma_{2\omega} \alpha_{2\omega})y} \cos(\Delta k \cdot y)]. \tag{6}$$

In PM conditions, the SH efficiency η for a given propagation distance y, as a function of N, is very well approximated by the term $\Gamma_{112}{}^2/(2\Gamma_\omega \alpha_\omega - \Gamma_{2\omega} \alpha_{2\omega})^2$ of Eq. (6), as it can be seen in Fig. 8. Therefore, the drop of the conversion efficiency for increasing N, can be explained by the increasing difference between the overlap factors of the pump and second harmonic fields.
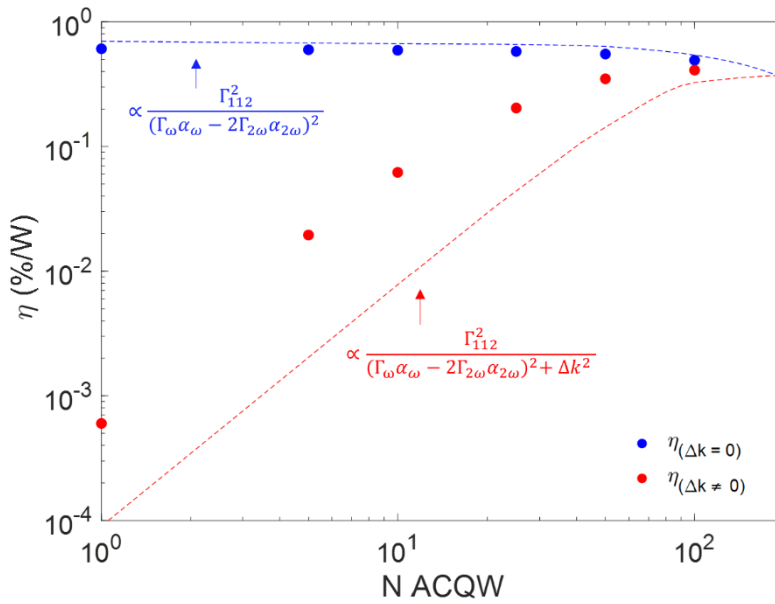

Fig. 8. SHG peak efficiency as a function of the number N of ACQW calculated by numeric integration of Eq. (2) and (3) (blue dots for PM, red dots for non-PM) compared with the trends calculated by considering the dominant term of Eq. (6) (blue dashed line for PM, red dashed line for non-PM).

In non-PM conditions, we observe a qualitative agreement between the SH efficiency as a function of N and the term $\Gamma_{112}{}^2/((2\Gamma_\omega \alpha_\omega - \Gamma_{2\omega} \alpha_{2\omega})^2 + \Delta k^2)$ of Eq. (6) (see Fig. 8).

So, as opposite to the previous case, the drop of the SH efficiency for decreasing N can be mainly ascribed to the phase mismatch Δk, which increases as N decreases (See Tab.1), strongly damping $\eta(y)$ for small N. Here it should be stated that the simulations have been performed neglecting the saturation of SHG at high pump intensities, which typically occurs at 0 MW/cm^2.

7.   Comparison with other material platforms

In this Section, we will compare the theoretical results obtained in this work with state-of-the-art nonlinear materials, limiting the discussion to those suitable for waveguide integration. Conventional non-linear crystals as LiNbO3 and KTP can achieve impressive nonlinear conversion efficiencies by leveraging on very long propagation distances, typically several mm, made possible by the negligible absorption coefficient. On the other hand, artificial nonlinear materials such as the Ge/SiGe ACQWs provides much higher $\chi^{(2)}$ values, but the rather strong linear absorption associated to the ISBTs limits the viable propagation distances to a few hundreds of μm. In such materials the conversion efficiency does not scale with the square of the propagation length L, as in conventional non-linear crystals, so the widely used figure of merit for SHG efficiency, expressed in $\%W^{-1}L^{-2}$, cannot be applied here. To make a meaningful comparison, taking into account also the significantly different dependence of artificial and conventional non-linear materials over the propagation length, we will use the power normalized conversion efficiency η, expressed in $\%W^{-1}$. The highest SHG efficiency reported so far for LNOI is $\eta = 2.41\%/W$ [24] obtained in a periodically-poled, 4 mm long WG, pumped around 1.55 μm. Another interesting material is GaAs-on-insulator, where the rather high $\chi^{(2)}$ of 150 pm/V has been harnessed to reach an impressive $\eta = 39.5\%/W$ in 2.9 mm WG pumped at $\lambda = 2$ μm [25]. Strain-induced symmetry breaking has been exploited in silicon-on-insulator (SOI) with silicon nitride stressors to generate SH. In this work [19] a 2 mm long WG pumped at 2.1 μm has shown SHG with an input power normalized efficiency $\eta = 8 \times 10^{-6}\%/W$. In all these works, the waveguiding structure relies on the high index contrast provided by the SiO2 layer, which is highly lossy beyond $\lambda = 4$ μm. Consequently, in the actual configuration, all these material platforms have been used to demonstrate SHG only in the short-wave part of the MIR. It should also be mentioned that other integrated devices such as high-Q micro-ring resonators have been employed to drastically boost the conversion efficiency with respect to simple straight WGs [18,49]. Finally, we compare our results with those obtained by another artificial non-linearity [45]. In this work, De Leonardis and Soref theoretically investigated Si/GaP ACQWs in WG configurations, obtaining $\eta = 1.68\%/W$ in few-μm long WGs, by considering a pump wavelength of $\lambda = 4.2$ μm.

8.   Conclusions

We have studied SHG generation in non-linear Ge-rich WGs, embedding an active region made of p-type ACQWs, designed to feature a double degenerate ISB resonance. Our numerical analysis provides a physical interpretation for the dependence of the output SH field in terms of overlap factors and absorption effects. In particular, to individuate an optimal WG design, we have investigated the competition between the giant second order susceptivity and the absorption of the SHG photons, caused by the ISBTs occurring in the Ge/SiGe ACQWs. Interestingly we found that, by using a large number of ACQWs, high conversion efficiencies could be obtained even in absence of phase-matching. From a technological point of view, this is an important aspect, since achieving the phase matching condition in this material system is feasible but challenging, especially if pursued by WG shape modulation, which complicates the fabrication process and enhance the propagation losses. Furthermore, our analysis shows how the number of ACQW periodic modules can be engineered to achieve small optimal propagation distances with tolerable losses in the SHG conversion efficiency. In conclusion, our findings indicate that Ge/SiGe ACQWs can compete with other state-of-the-art non-linear material platforms in terms of conversion efficiency, providing also the capability to work in the long-wave part of the MIR. Moreover, the prompt compatibility with the well-established SiGe photonic platform and the possibility to realize very compact devices makes this material extremely interesting for the development of nonlinear photonic building blocks in MIR PICs.

Disclosures. The authors declare no conflicts of interest.

Data availability. Data underlying the results presented in this paper are not publicly available at this time but may be obtained from the authors upon reasonable request.

References

1. V. Mittal, M. Nedeljkovic, L. G. Carpenter, A. Z. Khokhar, H. M. H. Chong, G. Z. Mashanovich, P. N. Bartlett, and J. S. Wilkinson, "Waveguide Absorption Spectroscopy of Bovine Serum Albumin in the Mid-Infrared Fingerprint Region," ACS Sens. **4**(7), 1749–1753 (2019).
2. M. Yu, Y. Okawachi, A. G. Griffith, M. Lipson, and A. L. Gaeta, "Microfluidic mid-infrared spectroscopy via microresonator-based dual-comb source," Opt. Lett. **44**(17), 4259–4262 (2019).
3. A. Vasiliev, A. Malik, M. Muneeb, B. Kuyken, R. Baets, and G. Roelkens, "On-Chip Mid-Infrared Photothermal Spectroscopy Using Suspended Silicon-on-Insulator Microring Resonators," ACS Sens. **1**(11), 1301–1307 (2016).
4. Y.-C. Chang, P. Wägli, V. Paeder, A. Homsy, L. Hvozdara, P. van der Wal, J. Di Francesco, N. F. de Rooij, and H. Peter Herzig, "Cocaine detection by a mid-infrared waveguide integrated with a microfluidic chip," Lab Chip **12**(17), 3020–3023 (2012).
5. B. G. Lee, M. A. Belkin, R. Audet, J. MacArthur, L. Diehl, C. Pflügl, F. Capasso, D. C. Oakley, D. Chapman, A. Napoleone, D. Bour, S. Corzine, G. Höfler, and J. Faist, "Widely tunable single-mode quantum cascade laser source for mid-infrared spectroscopy," Appl. Phys. Lett. **91**(23), 231101 (2007).
6. P. T. Lin, S. W. Kwok, H. Y. G. Lin, V. Singh, L. C. Kimerling, G. M. Whitesides, and A. Agarwal, "Mid-Infrared spectrometer using opto-nanofluidic slot-waveguide for label-free on-chip chemical sensing," Nano Lett. **14**(1), 231–238 (2014).
7. M. Borghi, C. Castellan, S. Signorini, A. Trenti, and L. Pavesi, "Nonlinear silicon photonics," J. Opt. **19**(9), 093002 (2017).
8. H. Lin, Z. Luo, T. Gu, L. C. Kimerling, K. Wada, A. Agarwal, and H. Juejun, "Mid-infrared integrated photonics on silicon: a perspective," Nanophotonics **7**(2), 393–420 (2017).
9. R. W. Boyd, *Nonlinear Optics*. Academic Press, 2002.
10. S. Liu, A. K. Gordon, J. L. Reno, M. B. Sinclair, and I. Brener, "III–V Semiconductor nano-resonators-a new strategy for passive, active and nonlinear all-dielectric metamaterials," Advanced Optical. Materials **4**(10), 1457–1462 (2016).
11. M. Zhang, B. Buscaino, C. Wang, A. Shams-Ansari, C. Reimer, R. Zhu, J. M. Kahn, and M. Loncar, "Broadband electro-optic frequency comb generation in a lithium niobate microring resonator," Nature **568**(7752), 373–377 (2019).
12. D. J. Jones, S. A. Diddams, J. K. Ranka, A. Stentz, R. S. Windeler, J. L. Hall, and S. T. Cundiff, "Carrier-envelope phase control of femtosecond mode-locked lasers and direct optical frequency synthesis," Science **288**(5466), 635–639 (2000).
13. S. Mosca, I. Ricciardi, M. Parisi, P. Maddaloni, L. Santamaria, P. De Natale, and M. De Rosa, "Direct generation of optical frequency combs in nonlinear cavities," Nanophotonics **5**, 316–331 (2016).
14. P.P. Absil, P. Verheyen, P. De Heyn, M. Pantouvaki, G. Lepage, J. De Coster, and J. Van Campenhout, "Silicon photonics integrated circuits: a manufacturing platform for high density; low power optical I/O's," Opt. Express **23**(7), 9369–9378 (2015).
15. A. E.-J. Lim, J. Song, Q. Fang, C. Li, X. Tu, N. Duan, K. K. Chen, R. P.-C. Tern, and R. T. Y. Liow, "Review of silicon photonics foundry efforts," IEEE J. Sel. Top. Quantum Electron. **20**(4), 405–416 (2014).
16. R. Franchi, C. Castellan, M. Ghulinyan, and L. Pavesi, "Second-harmonic generation in periodically poled silicon waveguides with lateral p-i-n junctions," Opt. Lett. **45**(12), 3188–3191 (2020).
17. T. Ning, H. Pietarinen, O. Hyvarinen, J. Simonen, G. Genty, and M. Kauranen, "Strong second-harmonic generation in silicon nitride films," Appl. Phys. Lett. **100**(16), 161902 (2012).
18. X. Lu, G. Moille, R. Ashutosh, D. A. Westly, and K. Srinivasan, "Efficient photoinduced second-harmonic generation in silicon nitride photonics," Nat. Photonics **15**(2), 131–136 (2021).
19. M. Cazzanelli, F. Bianco, E. Borga, G. Pucker, M. Ghulinyan, E. Degoli, E. Luppi, V. Veniard, S. Ossicini, D. Modotto, S. Wabnitz, R. Pierobon, and L. Pavesi, "Second-harmonic generation in silicon waveguides strained by silicon nitride," Nat. Mater. **11**(2), 148–154 (2012).
20. D. J. Moss, R. Morandotti, A. L. Gaeta, and M. Lipson, "New CMOS-compatible platforms based on silicon nitride and Hydex for nonlinear optics," Nat. Photonics **7**(8), 597–607 (2013).
21. C. Y. Wang, T. Herr, P. Del'Haye, A. Schliesser, J. Hofer, R. Holzwarth, T. W. Hansch, N. Picque, and T. J. Kippenberg, "Mid-infrared optical frequency combs at 2.5 µm based on crystalline microresonators," Nat. Commun. **4**(1), 1345 (2013).
22. A. L. Gaeta, M. Lipson, and T. J. Kippenberg, "Photonic-chip-based frequency combs," Nat. Photonics **13**(3), 158–169 (2019).
23. S. Fathpour, "Heterogeneous nonlinear integrated photonics," IEEE J. Quantum Electron. **54**(6), 1–16 (2018).
24. C. Wang, C. Langrock, A. Marandi, M. Jankowsky, M. Zhang, B. Desiatov, M. M. Fejer, and M. Loncar, "Ultrahigh-efficiency wavelength conversion in nanophotonic periodically poled lithium niobate waveguides," Optica **5**(11), 1438–1441 (2018).
25. E. J. Stanton, J. Chiles, N. Nader, G. Moody, N. Volet, L. Chang, J. E. Bowers, S. W. Nam, and R. P. Mirin, "Efficient second harmonic generation in nanophotonic GaAs-on-insulator waveguides," Opt. Express **28**(7), 9521–9532 (2020).

26. S. V. Makarov, M. I. Petrov, U. Zywietz, V. Milichko, D. Zuev, N. Lopanitsyna, A. Kuskin, I. Mukhin, G. Zograf, E. Ubyivok, D. A. Smirnova, S. Starikov, B. N. Chichkov, and Y. S. Kivshar, "Efficient Second-Harmonic Generation in Nanocrystalline Silicon Nanoparticles," Nano Lett. **17**(5), 3047–3053 (2017).

27. M. Fischer, A. Riede, K. Gallacher, J. Frigerio, G. Pellegrini, M. Ortolani, D. J. Paul, G. Isella, A. Leitenstorfer, P. Biagioni, and D. Brida, "Plasmonic mid-infrared third harmonic generation in germanium nanoantennas," Light: Sci. Appl. **7**(1), 106 (2018).

28. J. Frigerio, C. Ciano, J. Kuttruff, A. Mancini, A. Ballabio, D. Chrastina, V. Falcone, M. De Seta, L. Baldassarre, J. Allerbeck, D. Brida, L. Zeng, E. Olsson, M. Virgilio, and M. Ortolani, "Second Harmonic Generation in Germanium Quantum Wells for Nonlinear Silicon Photonics," ACS Photonics **8**(12), 3573–3582 (2021).

29. S. Li and J. Khurgin, "Second-order nonlinear optical susceptibility in p-doped asymmetric quantum wells," Appl. Phys. Lett. **62**(15), 1727–1729 (1993).

30. E. Rosencher, A. Fiore, B. Vinter, V. Berger, P. Bois, and J. Nagle, "Quantum Engineering of Optical Nonlinearities," Science **271**(5246), 168–173 (1996).

31. K. L. Vodopyanov, K. O'Neill, G. B. Serapiglia, and C. C. Phillips, "Phase-matched second harmonic generation in asymmetric double quantum wells," Appl. Phys. Lett. **72**(21), 2654–2656 (1998).

32. J. Lee, M. Tymchenko, C. Argyropoulos, P. Y. Chen, F. Lu, F. Demmerle, G. Boehm, M. C. Amann, A. Alu, and M. A. Belkin, "Giant nonlinear response from plasmonic metasurfaces coupled to intersubband transitions," Nature **511**(7507), 65–69 (2014).

33. R. Sarma, J. Xu, D. de Ceglia, L. Carletti, S. Campione, J. Klem, M. B. Sinclair, M. A. Belkin, and I. Brener, "An All-Dielectric Polaritonic Metasurface with a Giant Nonlinear Optical Response," Nano Lett. **22**(3), 896–903 (2022).

34. R. Sarma, J. Xu, D. de Ceglia, L. Carletti, J. Klem, M. A. Belkin, and I. Brener, "Control of second-harmonic generation in all-dielectric intersubband metasurfaces by controlling the polarity of $\chi^{(2)}$," Opt. Express **30**(19), 34533–34544 (2022).

35. R. Sarma, D. de Ceglia, N. Nookala, M. A. Vincenti, S. Campione, O. Wolf, M. Scalora, M. B. Sinclair, M. A. Belkin, and I. Brener, "Broadband and Efficient Second-Harmonic Generation from a Hybrid Dielectric Metasurface/Semiconductor Quantum-Well Structure," ACS Photonics **6**(6), 1458–1465 (2019).

36. J. Frigerio, A. Ballabio, M. Ortolani, and M. Virgilio, "Modeling of second harmonic generation in hole-doped silicon-germanium quantum wells for mid-infrared sensing," Opt. Express **26**(24), 31861–31872 (2018).

37. M. Virgilio and G. Grosso, "Valence and conduction intersubband transitions in SiGe, Ge-rich, quantum wells on [001] $Si_{0.5}Ge_{0.5}$ substrates: A tight-binding approach," J. Appl. Phys. **100**(9), 093506 (2006).

38. M. Virgilio and G. Grosso, "Valley splitting and optical intersubband transitions at parallel and normal incidence in [001]-Ge/SiGe quantum wells," Phys. Rev. B **79**(16), 165310 (2009).

39. R. A. Soref and B. R. Bennet, "Electrooptical effects in Silicon," IEEE J. Quantum Electron. **23**(1), 123–129 (1987).

40. M. Nedeljkovic, R. Soref, and G. Z. Mashanovich, "Predictions of Free-Carrier Electroabsorption and Electrorefraction in Germanium," IEEE Photonics J. **7**(3), 1–14 (2015).

41. M. Nedeljkovic, R. Soref, and G. Z. Mashanovich, "Free-carrier electrorefraction and electroabsorption modulation predictions for silicon over the 1.3-14 µm infrared wavelength range," IEEE Photonics J. **3**(6), 1171–1180 (2011).

42. P. Chaisakul, D. Marris-Morini, J. Frigerio, D. Chrastina, M.-S. Rouifed, S. Cecchi, P. Crozat, G. Isella, and L. Vivien, "Integrated germanium optical interconnects on silicon substrates," Nat. Photonics **8**(6), 482–488 (2014).

43. J. M. Ramirez, Q. Liu, V. Vakarin, J. Frigerio, A. Ballabio, X. Le Roux, D. Bouville, L. Vivien, G. Isella, and D. Marris-Morini, "Graded SiGe waveguides with broadband low-loss propagation in the mid-infrared," Opt. Express **26**(2), 870–877 (2018).

44. F. De Leonardis and R. A. Soref, "Efficient Second-Harmonic Generation in Si-GaP Asymmetric Coupled-Quantum-Well Waveguides," J. Lightwave Technol. **40**(9), 2959–2964 (2022).

45. G. P. Agrawal, *Nonlinear Fiber Optics*, 3rd ed., Academic Press, San Diego, California, CA, USA, pp. 431–432, ch.10, 2001.

46. M. Montesinos-Ballester, V. Vakarin, Q. Liu, X. Le Roux, J. Frigerio, A. Ballabio, A. Barzaghi, C. Alonso-Ramos, L. Vivien, G. Isella, and D. Marris-Morini, "Ge-rich SiGe waveguides and interferometers from 5 to 11 µm wavelength range," Opt. Express **28**(9), 12771–12779 (2020).

47. G. Almogy, M. Segev, and A. Yariv, "Intersubband-trnasitions-induced phase matching," Opt. Lett. **19**(16), 1192 (1994).

48. A. Rao, J. Chiles, S. Khan, S. Toroghi, M. Malinowski, G.-F. Camacho-Gonzalez, and S. Fathpour, "Second Harmonic Generation in single-mode integrated waveguides based on mode-shape modulation," Appl. Phys. Lett. **110**(11), 111109 (2017).

49. J. Lu, B. J. B. Surya, X. Liu, A. W. Bruch, Z. Gong, Y. Xu, and H. X. Tang, "Periodically poled thin-film lithium niobate microring resonators with a second-harmonic generation efficiency of 250,000 %/W," Optica **6**(12), 1455–1460 (2019).